



HAL
open science

CRESCENT-1D: A 1D solver of coupled charge and light transport in heterostructures for the design of near-field thermophotonic engines

Julien Legendre, Pierre-Olivier Chapuis

► **To cite this version:**

Julien Legendre, Pierre-Olivier Chapuis. CRESCENT-1D: A 1D solver of coupled charge and light transport in heterostructures for the design of near-field thermophotonic engines. 2024. hal-04749430v1

HAL Id: hal-04749430

<https://hal.science/hal-04749430v1>

Preprint submitted on 23 Oct 2024 (v1), last revised 25 Oct 2024 (v2)

HAL is a multi-disciplinary open access archive for the deposit and dissemination of scientific research documents, whether they are published or not. The documents may come from teaching and research institutions in France or abroad, or from public or private research centers.

L'archive ouverte pluridisciplinaire **HAL**, est destinée au dépôt et à la diffusion de documents scientifiques de niveau recherche, publiés ou non, émanant des établissements d'enseignement et de recherche français ou étrangers, des laboratoires publics ou privés.

CRESCENT-1D: A 1D solver of coupled charge and light transport in heterostructures for the design of near-field thermophotonic engines

Julien Legendre, Pierre-Olivier Chapuis

Abstract—Thermophotonic devices are radiative heat engines in which the exchange of electroluminescent radiation between a heated light-emitting diode and a cool photovoltaic cell allows for the conversion of heat into electrical power. Here, we introduce CRESCENT-1D, the solver we have developed to simulate the performance of one-dimensional thermophotonic systems, which is made publicly available on GitHub. It couples photon transport in the far or near field, based on the fluctuational electrodynamics framework, and charge transport in heterostructures, modelled with the drift-diffusion and Poisson equations. We include both thermionic emission and charge carrier tunnelling to precisely model charge transport at heterointerfaces, while the photon chemical potential is computed in a self-consistent manner between the radiative and electrical sections of the solver. Compared to simpler formulations, these models provide accurate results at high voltages, which is essential to achieve high power output. The capabilities of CRESCENT-1D are illustrated with an optimised InGaP/InGaAs thermophotonic heterostructure, whose maximum power reaches 1.6 W.cm^{-2} for an efficiency of 19.7% considering a 300 K temperature difference between the light-emitting diode and the photovoltaic cell. This solver makes it possible for anyone to design various categories of optoelectronic structures (thermophotonics, light-emitting diode, thermophotovoltaics, thermoradiative, etc.), and represent an important step in the development of near-field radiative heat engines.

Index Terms—Optoelectronic device simulation, Thermophotonics, Charge transport in semiconductors, Near-field radiative heat transfer, Heterostructures.

I. INTRODUCTION

THERMOPHOTONIC (TPX) systems are a kind of dual radiative heat engine [1] in which a heated light-emitting diode (LED) is coupled radiatively and electrically to a photovoltaic (PV) cell at ambient temperature [2]. When supplied with electricity, the LED is able to emit electroluminescent radiation towards the PV cell with above-unity wall-plug

efficiency, defined as the ratio of the emitted radiative flux and the incoming electrical power. This can happen because part of the radiative energy comes from the crystalline lattice, similarly to electroluminescent (EL) cooling [3]–[6]. Under certain conditions, the PV cell can therefore generate more electrical power than the LED needs, enabling TPX conversion. Such systems can be understood as evolutions of thermophotovoltaic (TPV) devices, in which the hot emitter remains passive [7]–[10]. While efficient for high heat source temperature, TPV power output strongly decreases when operating closer to ambient, being limited by Planck’s law. This is not the case with TPX devices, since the radiation exchanged is electroluminescent: this makes them highly appealing for low temperature applications, e.g. for energy harvesting.

Initially proposed at the beginning of the century [2], [11], research on TPX devices mainly started in the end of the 2010s [12]–[18], owing to the simultaneous development of TPV and EL cooling. In most of the literature, devices operate in the near field (NF), allowing additional photons to travel between the LED and the PV cell through tunnelling and leading to a significant power enhancement [19], [20]. All these papers also share a similar electrical model, based on detailed balance of photon and charge carriers. The strength of such models lies in their ability to provide performance bounds and insight into the impact of key parameters, while maintaining relative simplicity. However, being inherently 0D, they do not allow estimating the performance of realistic structures which is essential to drive the design of experimental prototypes.

To determine the performance of structures, charge transport shall be modelled. For energy conversion applications such as TPV, drift-diffusion models are almost systematically selected, although other models are also available [21]. These models can be further segregated depending on the systems they are able to represent, either homostructures only [22], [23] or both homo- and heterostructures [24]–[29]. In previous papers, we studied NF-TPX systems composed of 1D homostructures with an in-house radiative and electrical solver, and notably pinpointed the importance of reaching close-to-unity LED quantum efficiency [30], [31]. Achieving such values requires very high carrier selectivity, which can practically only be attained with heterostructures.

In the current paper, we introduce CRESCENT-1D (Coupled Radiative and Electrical Solver for Efficient Near-field Thermophotonics in 1D), the solver we have developed in MAT-

Manuscript submitted October xx, 2024. This work has received funding from the European Union’s Horizon 2020 research and innovation programme under Grant Agreement No. 951976 (TPX-Power project).

J. Legendre was with Univ Lyon, CNRS, INSA-Lyon, Université Claude Bernard Lyon 1, CETHIL UMR5008, F-69621, Villeurbanne, France. He is now with ICFO-Institut de Ciències Fotoniques, Barcelona, Spain (e-mail: julien.legendre@icfo.eu).

P.-O. Chapuis is with Univ Lyon, CNRS, INSA-Lyon, Université Claude Bernard Lyon 1, CETHIL UMR5008, F-69621, Villeurbanne, France (e-mail: pierre-olivier.chapuis@insa-lyon.fr).

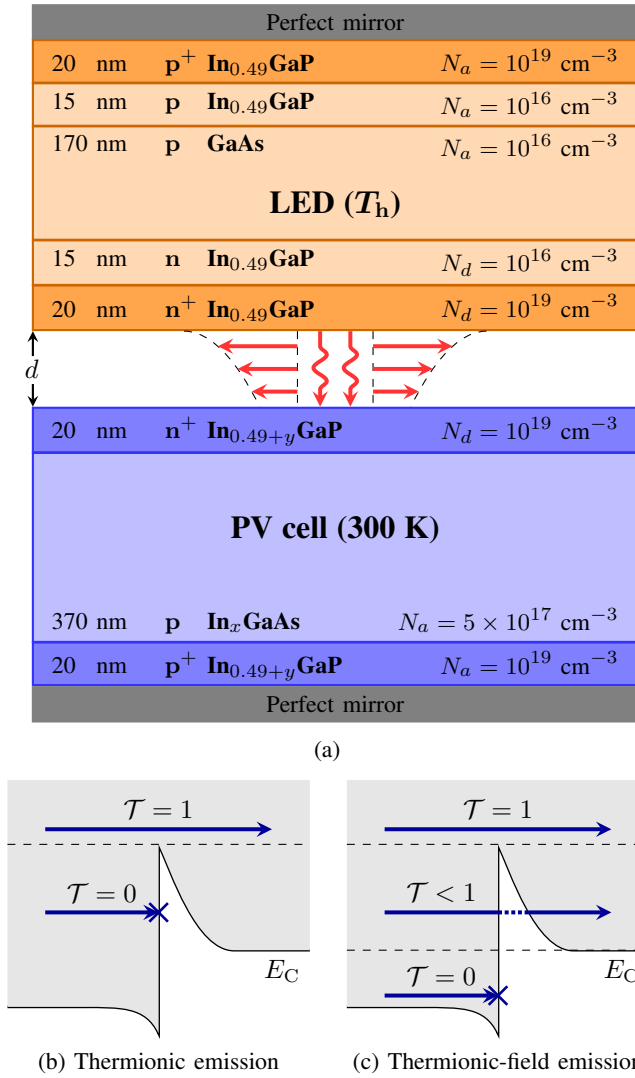


Fig. 1: (a) Heterostructure-based InGaAs/InGaP TPX device considered throughout the article, where fractions x and y depend on the heat source temperature T_h . (b,c) Charge carrier transmission models at potential barriers.

LAB to model the performance of NF-TPX heterostructures. It is made publicly available on [GitHub](#). This code, apart from being the first to simulate charge transport in heterostructures for complete TPX devices, also includes features that are rarely present in comparable codes, such as self-consistent photon chemical potential estimation and photon tunnelling. Thereafter, we present the models considered, along with the underlying equations and the methods used to solve them. The capabilities of CRESCENT-1D, which matches well SCAPS [24] results in the case of a simple system, are then illustrated considering an optimised NF-TPX system based on InGaP/InGaAs heterostructures (see Fig. 1a). The device performance is presented at the end of the article.

II. MODELS AND RESOLUTION METHODS

CRESCENT-1D can be divided into two main constitutive blocks. In the first block, fluctuational electrodynamics is

used to calculate the photonic transmission coefficient between each point in the LED and in the PV cell. The radiative recombination-generation rate in both components can then be computed, and used to solve the drift-diffusion equations along with the Poisson and continuity equations in the second block.

A. Transmission of near-field radiation

The calculation of the photon transmission coefficient \mathcal{T} between 1D bodies in the near field is performed in a way similar to previous studies of TPV (see e.g. [22], [32]) and TPX systems (see e.g. [12], [30]), and will therefore be kept brief. We follow the method proposed in [33]. To compute the radiative generation and recombination rates, we ultimately need the local emission and absorption rates. These terms do not directly depend on \mathcal{T} , but rather on its derivative with respect to the emission position, which can be expressed as

$$\frac{d\mathcal{T}}{dz_m} = 4k_0^2 \varepsilon''_{r,m} \operatorname{Re} \left\{ i \begin{bmatrix} g_{mn,\rho\rho}^{\mathcal{E}} g_{mn,\theta\rho}^{\mathcal{H}*} \\ + g_{mn,\rho z}^{\mathcal{E}} g_{mn,\theta z}^{\mathcal{H}*} \\ - g_{mn,\theta\theta}^{\mathcal{E}} g_{mn,\theta\rho}^{\mathcal{H}*} \end{bmatrix} \right\}. \quad (1)$$

$k_0 = \omega/c$ represents the vacuum wavenumber, $\varepsilon''_{r,m}$ is the imaginary part of the dielectric function of the emitter and $g_{mn,xy}$ is the xy Weyl component of the Green tensor between emitting layer m and absorbing layer n , either relative to the electric field \mathcal{E} or to the magnetic field \mathcal{H} . These components are computed using a scattering matrix formalism, and depend on the angular frequency ω , the parallel component of the wavevector k_ρ , and the emitting and absorbing positions z_m and z_n . In the following, we rather use the transmission factor \mathcal{F} for simplicity, expressed as

$$\mathcal{F} = \frac{1}{4\pi^2} \int_0^\infty \frac{d\mathcal{T}}{dz_m} k_\rho dk_\rho. \quad (2)$$

This quantity is given per unit thickness of the emitter: therefore, the radiative generation and recombination rates cannot be expressed the same way in the emitter and the absorber. The net recombination-generation rate r caused by the radiative exchanges between the emitting layer m and the absorbing layer n , respectively for layer m and n , is

$$r_{\text{rad},m}(z_m) = \int_0^\infty (f_{\text{BE}}(\omega, \mu_m, T_m) - f_{\text{BE}}(\omega, \mu_n, T_n)) \times (\mathcal{F}(\omega, z_m, z_{n,\text{in}}) - \mathcal{F}(\omega, z_m, z_{n,\text{out}})) d\omega, \quad (3a)$$

$$r_{\text{rad},n}(z_n) = \int_0^\infty (f_{\text{BE}}(\omega, \mu_n, T_n) - f_{\text{BE}}(\omega, \mu_m, T_m)) \times \frac{d}{dz_n} \left(\int_{z_m} \mathcal{F}(\omega, z_m, z_n) dz_m \right) d\omega. \quad (3b)$$

In these expressions $z_{n,\text{in}}$ and $z_{n,\text{out}}$ correspond to the spatial boundaries of layer n , respectively closer and further away from the emitting layer. $f_{\text{BE}}(\omega, \mu, T) = [\exp((\hbar\omega - \mu)/k_B T) - 1]^{-1}$ is the generalised Bose-Einstein distribution, which is a function of the emitting layer temperature T and of the photon chemical potential μ . The way μ is computed will be discussed in Section II-C.

In the following, we will consider that there is a net photon flux only between layers of the LED and the PV cell, i.e. that the photon flux is zero between two layers of the same component. This is not strictly true: although the temperature is supposed to be constant throughout a component, the chemical potential of emitted photons varies spatially. Still, these variations are relatively slow (as later shown in Fig. 4, panel (b)), so that internal photon transfer can be neglected as a first-order approximation. Also, it shall be noted that computing such internal transfer is not straightforward, since the above equations diverge for two arbitrarily close bodies (see Section I of Supp. Mat.). If one simple solution could be to consider only modes which are propagating inside the component, the rigorous calculation of this internal transfer probably requires to relax the locality approximation [34], [35], i.e. by using ω - and k_ρ -dependent dielectric functions.

B. Electrical characterisation of optoelectronic components

1) *Within a layer*: In each layer of the optoelectronic components, charge transport is modelled using the drift-diffusion equations for electron and holes, along with Poisson equation to ensure consistency between charge density and electric field, and continuity equation to satisfy charge conservation. The classical expression of these equations is provided frequently in the literature (see e.g. [21], [25], [31]) and will therefore not be recalled here. Rather, we express them in the so-called Slotboom formulation [36], which will be the one preferred to solve them. The drift-diffusion equations are then:

$$J_n^{dd}(z) = eD_n(z)n_{i,\text{ref}}e^{\xi_n}e^{+\Psi(z)}\frac{d\Phi_n}{dz}(z), \quad (4a)$$

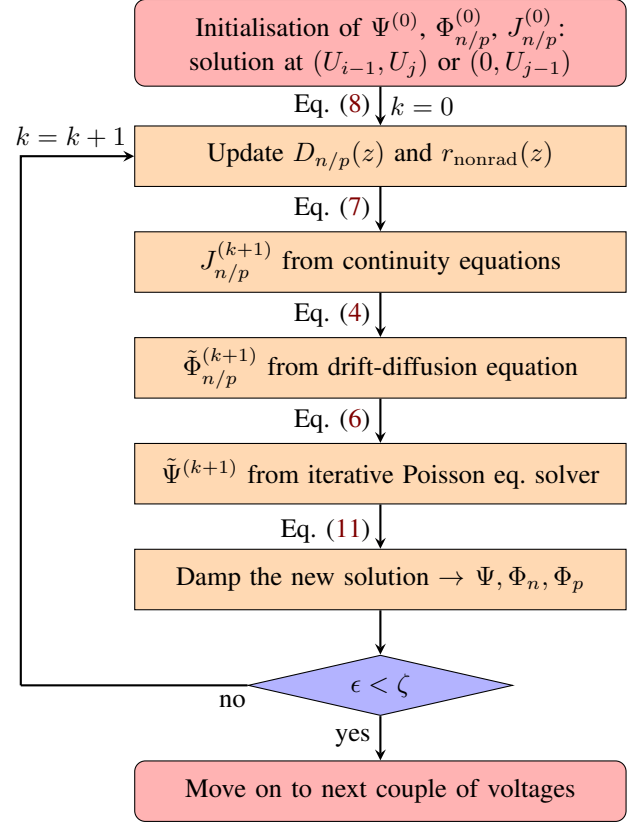
$$J_p^{dd}(z) = -eD_p(z)n_{i,\text{ref}}e^{\xi_p}e^{-\Psi(z)}\frac{d\Phi_p}{dz}(z). \quad (4b)$$

J_i^{dd} is the drift-diffusion current relative to charge carrier i , e is the elementary charge, $D_i = \mu_i k_B T / e$ is the charge carrier diffusivity and μ_i its mobility. $\Psi = eV / k_B T$ is the normalised electrostatic potential, and $\Phi_n = \exp(E_{Fn} / k_B T)$ and $\Phi_p = \exp(-E_{Fp} / k_B T)$ are the Slotboom variables, E_{Fi} being the quasi-Fermi level related to carrier i . Note that in this formulation, the energy reference of the electrostatic potential energy $-eV$ is different from that of the quasi-Fermi levels [37]. In heterostructures, the electronic properties of the various materials can be different. To take that into account, one material is set to be the reference; its intrinsic carrier density $n_{i,\text{ref}}$ is used in the above equations, and the terms ξ_i allows accounting for the deviation in properties in comparison to this reference [38]. They always equal 0 for the reference material, and are defined for any material m as

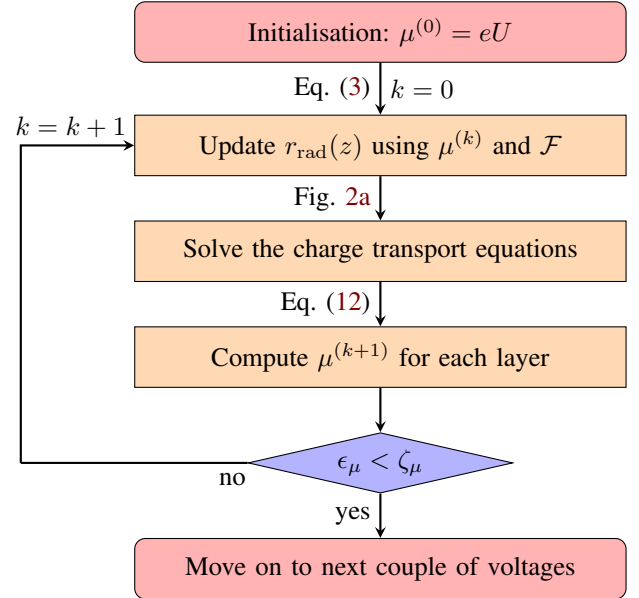
$$\xi_n = \frac{\chi_m - \chi_{\text{ref}}}{k_B T} + \frac{1}{2} \ln \left(\frac{N_{C,m}}{N_{C,\text{ref}}} \right), \quad (5a)$$

$$\xi_p = -\frac{\chi_m - \chi_{\text{ref}}}{k_B T} - \frac{E_{g,m} - E_{g,\text{ref}}}{2k_B T} + \frac{1}{2} \ln \left(\frac{N_{V,m}}{N_{V,\text{ref}}} \right), \quad (5b)$$

where χ is the electron affinity, E_g is the bandgap energy, and N_C and N_V are respectively the effective density of states in



(a)



(b)

Fig. 2: (a) Flowchart of the drift-diffusion solver for heterostructures at $(U_{\text{LED}}, U_{\text{PV}}) = (U_i, U_j)$. (b) Flowchart of radiative and electrical solver coupling for self-consistent photon chemical potential estimation.

the conduction and valence bands. Using the aforementioned quantities, electron and hole densities are respectively equal to $n = n_{i,\text{ref}} e^{\xi_n} e^{\Psi(z)} \Phi_n(z)$ and $p = n_{i,\text{ref}} e^{\xi_p} e^{-\Psi(z)} \Phi_p(z)$.

Poisson's equation can be written as

$$\frac{d^2\Psi}{d\tilde{z}^2}(\tilde{z}) = e^{\xi_n} e^{\Psi(\tilde{z})} \Phi_n(\tilde{z}) - e^{\xi_p} e^{-\Psi(\tilde{z})} \Phi_p(\tilde{z}) + \tilde{N}_{\text{dop}}(\tilde{z}), \quad (6)$$

\tilde{z} being the position z normalised by the reference material intrinsic Debye length $\sqrt{\varepsilon_{\text{rs,ref}} \varepsilon_{\text{v}} k_{\text{B}} T / e^2 n_{i,\text{ref}}}$ with $\varepsilon_{\text{rs,ref}}$ the static dielectric constant of the reference material and ε_{v} the vacuum permittivity. $\tilde{N}_{\text{dop}} = (N_{\text{a}} - N_{\text{d}}) / n_{i,\text{ref}}$ is the normalised doping level.

At last, continuity equations are

$$\frac{dJ_n}{dz}(z) = e \cdot r(z), \quad (7a)$$

$$\frac{dJ_p}{dz}(z) = -e \cdot r(z), \quad (7b)$$

J_i being the *total* current density related to carrier i . r is the net recombination-generation rate, which includes the contributions of radiative, Shockley-Read-Hall (SRH) and Auger events: $r = r_{\text{rad}} + r_{\text{SRH}} + r_{\text{Auger}}$. The two latter non-radiative contributions are computed from the following nonlinear expressions:

$$r_{\text{SRH}} = \frac{np - n_i^2}{\tau_n(p + n_i) + \tau_p(n + n_i)}, \quad (8a)$$

$$r_{\text{Auger}} = (C_n n + C_p p)(np - n_i^2), \quad (8b)$$

where τ_i is the SRH lifetime and C_i is the Auger recombination coefficient. The values selected for these parameters and for the other material properties previously mentioned are presented in Section II of Supp. Mat. Note that because of the absence of accurate data, the non-radiative coefficients used are those of GaAs at room temperature. A better estimation of the temperature and composition dependencies of these coefficients will be crucial for the accurate design of TPX structures [37].

2) At interfaces: Two different kinds of interfaces are considered: those with the electrical contacts, and those between two different semiconductors. We start with the former, which are modelled assuming that

- the surroundings of these interfaces are uncharged, leading to $d^2\Psi/d\tilde{z}^2(\tilde{z}) = 0$;
- the majority carriers are at equilibrium with the charge inside the contacts, i.e. $E_{\text{Fn}} = eU$ (U being the applied voltage) and $E_{\text{Fp}} = 0$;
- the minority carrier current is directly related to the surface recombination rate through

$$J_{\text{min}} = \pm e \frac{np - n_i^2}{\frac{1}{S_p}(n + n_i) + \frac{1}{S_n}(p + n_i)}, \quad (9)$$

S being the surface recombination velocity, and the sign of the right term depending on the carrier type.

At heterointerfaces, we assume that the total current density related to a carrier is continuous. These interfaces are supposed to be electrically neutral, which leads the electric displacement field $\mathbf{D} = \varepsilon_{\text{s}} \mathbf{E}$ to be also continuous. Lastly, we need to describe the variations of the quasi-Fermi levels - thus of Φ_n

and Φ_p - at the interface. CRESCENT-1D can simulate the system behaviour with three different models:

- continuity of the quasi-Fermi levels;
- thermionic emission model, in which charge carriers can be transmitted through a heterointerface only if their energy allows them surpassing the potential barrier (see Fig. 1b);
- thermionic-field emission model (in the WKB approximation), in which the carriers can also be transmitted by tunnelling through the barrier (see Fig. 1c).

For the two latter models, the discontinuity of the Slotboom variables is directly related to the total current density at the interface. For electrons, the relation is

$$J_n = AT^2(\eta_n + \varphi_n) e^{-\tilde{E}_{\text{C,max}}} (\Phi_n^+ - \Phi_n^-), \quad (10)$$

where $A = em_0 k_{\text{B}}^2 / 2\pi^2 \hbar^3$ is the Richardson constant for the free electron and $E_{\text{C}}(z)$ is the lower available energy in the conduction band. η_n and φ_n are parameters that respectively quantify transmission due to thermionic emission and charge tunnelling; in the second model, only the former phenomenon is included, thus $\varphi_n = 0$. These two parameters depend on material properties, φ_n being also a function of Ψ . When holes are considered, the above relation changes only slightly, with $e^{-\tilde{E}_{\text{C,max}}}$ being replaced by $e^{\tilde{E}_{\text{V,min}}}$ and η and φ having different expressions. Details on the derivation of this equation, and on the value of η and φ , are provided in Section III of Supp. Mat. These developments are based on [39]–[42].

As long as charge carrier tunnelling is neglected, charges can only travel inside a layer through drift or diffusion: the drift-diffusion current then equals the total current for each carrier. This is no longer the case when tunnelling is included, as it opens a new channel of charge transport. The tunnelling current shall thus be subtracted from the total current to obtain the drift-diffusion current used in Eq. (4).

3) Numerical resolution: With the model presented above, we now have five equations in the layer and at the inner boundaries to obtain the five unknowns of the problem: Ψ , J_n , J_p , Φ_n and Φ_p . However, these equations are coupled. Therefore, the system is solved iteratively, following the flowchart in Fig. 2a. For a given couple of applied voltage (U_i, U_j) respectively applied on the LED and the PV cell, each unknown is initialised using the closest solution already computed, i.e. the one obtained at

- (U_{i-1}, U_j) if $U_i > 0$,
- $(0, U_{j-1})$ if $U_i = 0$,
- equilibrium if both voltages are zero.

The classical Scharfetter-Gummel scheme is considered to solve the system [43], although in a modified version. In its standard formulation, the drift-diffusion and continuity equations are combined to obtain two second-order differential equations of the Slotboom variables, which are solved using finite difference and matrix inversion methods such as the tridiagonal matrix algorithm [22]. However, we observed that the total current was not spatially constant with this method, and thus preferred to rely on integration instead. Current densities and Slotboom variables are derived from the integration of the continuity and drift-diffusion equations

respectively, and from the boundary conditions mentioned above. The Poisson equation being non-linear, the electrostatic potential is calculated using another iterative process in which the linearised Poisson equation is repeatedly solved [21], [22].

The iterative resolution of the various equations does not guarantee to obtain a converged solution: if the changes between two iterations are too strong, the solver can indeed diverge. To limit this, we implemented in the solver the possibility to damp the solution of an iteration when convergence is difficult. Considering Ψ for instance, if $\Psi^{(k)}$ is the result of the previous iteration, and $\tilde{\Psi}^{(k+1)}$ the new result before damping, the final result is

$$\Psi^{(k+1)} = w\tilde{\Psi}^{(k+1)} + (1-w)\Psi^{(k)}, \quad (11)$$

where w is the weighting factor and is common for Ψ , Φ_n and Φ_p , the currents being not damped as they are the first to be computed in an iteration. Once the iteration is over, the maximum relative variations ϵ of n and p are calculated: if both are below the set tolerance ζ , the iterative process stops and moves to the next point in the voltage space.

C. Self-consistent estimation of the photon chemical potential

By definition, the chemical potential of photons emitted at a given location is equal to the difference in electron and hole quasi-Fermi level at this location: $\mu = E_{Fn} - E_{Fp}$. This underlines the coupling between radiation and charge transport: the simulation of charge transport requires knowledge on the radiative generation and recombination rates, the latter being dependent on μ and thus on charge transport results. To address this issue in modelling, two main solutions are generally considered: either assume that $\mu = eU$ [6], [12], [44], or express radiative recombinations using the common expression $r_{\text{rad}} = B_{\text{rad}}(np - n_i^2) = B_{\text{rad}}n_i^2(e^{\mu/k_B T} - 1)$, which can directly be used in the electrical solver to include the interdependency (B_{rad} being the radiative recombination coefficient which is generally considered to be a material property [22], [25], [27]). However, both of these methods involve approximations that do not hold well for NF-TPX or TPV systems made of heterostructures. Therefore, to ensure self-consistency between the radiative and electrical solvers without having to use any further approximations, the resolution is performed iteratively, following [32].

The corresponding flowchart is provided in Fig. 2b. Initially set to eU , μ is used to compute r_{rad} and subsequently to solve the drift-diffusion equations, as presented above. Once the electrical solver has converged, μ can then be updated using the newly calculated quasi-Fermi levels. In the best-case scenario, μ should be computed at each point of the spatial grid. However, doing so is detrimental to the computational time, as it increases the number of iterations needed to converge. To help convergence, we instead considered one unique value of μ per layer, which as we will see later on is a justified approximation. To ensure that the radiative emission is as precise as possible, the value of μ_m selected for each layer m is not the direct mean value of $E_{Fn} - E_{Fp}$ over the

layer thickness t_m , but rather the one that verifies

$$e^{\frac{\mu_m}{k_B T}} = \frac{1}{t_m} \int_{t_m} e^{\frac{E_{Fn}(z) - E_{Fp}(z)}{k_B T}} dz = \frac{1}{t_m} \int_{t_m} \Phi_n(z)\Phi_p(z) dz, \quad (12)$$

since r_{rad} varies as $e^{\mu/k_B T}$ as long as Boltzmann's approximation holds. The iterative solver stops once the maximum absolute variation of μ between two iterations ϵ_μ becomes lower than the set tolerance ζ_μ .

D. Neglected phenomena and approximations

Before moving on to the next section, it is worth mentioning that some physical phenomena are not yet implemented in CRESCENT-1D. These are mainly

- Joule losses inside the components and the electrical contacts, which could be accounted for in a heuristic manner without difficulty, e.g. as in [23];
- shading losses due to the front electrical contacts, which can be estimated by geometric means, i.e. by correcting the radiative heat transfer using the fraction of the area being shaded [23];
- parasitic absorption in the back mirror, which are currently neglected but could be included in the radiative solver;
- quantum interference phenomena, due to the use of the WKB approximation for estimating charge carrier tunnelling;
- reflection and transmission of tunnelling charge carriers at interfaces other than the one where tunnelling was initiated.

Additionally, the tunnelling probability is computed considering only the band structure close to the interface (in the following, up to 50 nm on each side) in order to limit computational cost (see Section III of Supp. Mat. for more details). Because the solver is one-dimensional, 2D phenomena are inherently excluded: among them, current crowding and surface recombinations at the component sides could play a non-negligible role. Our model relying on the Boltzmann approximation to simplify the Fermi-Dirac distribution normally followed by charge carriers, it is primarily made for the simulation of non-degenerate semiconductors.

III. RESULTS

CRESCENT-1D has been used to optimise the structure of one-dimensional NF-TPX devices to obtain the best electrical power output possible. This optimisation, performed with the MATLAB *surrogateopt* function, resulted in the structure illustrated in Fig. 1a. In order to focus on the solver capabilities, details on the optimisation process (e.g. on the material and the number of layers considered) are omitted in this article; they can be found in [37].

Thereafter, we present the typical results the solver can provide using the optimised structure, considering heat source and heat sink temperatures to be respectively equal to 600 K and 300 K. TPX systems are mostly considered for energy harvesting, for which heat supplied to the hot body can be considered free [45]: therefore, we will mostly focus on the

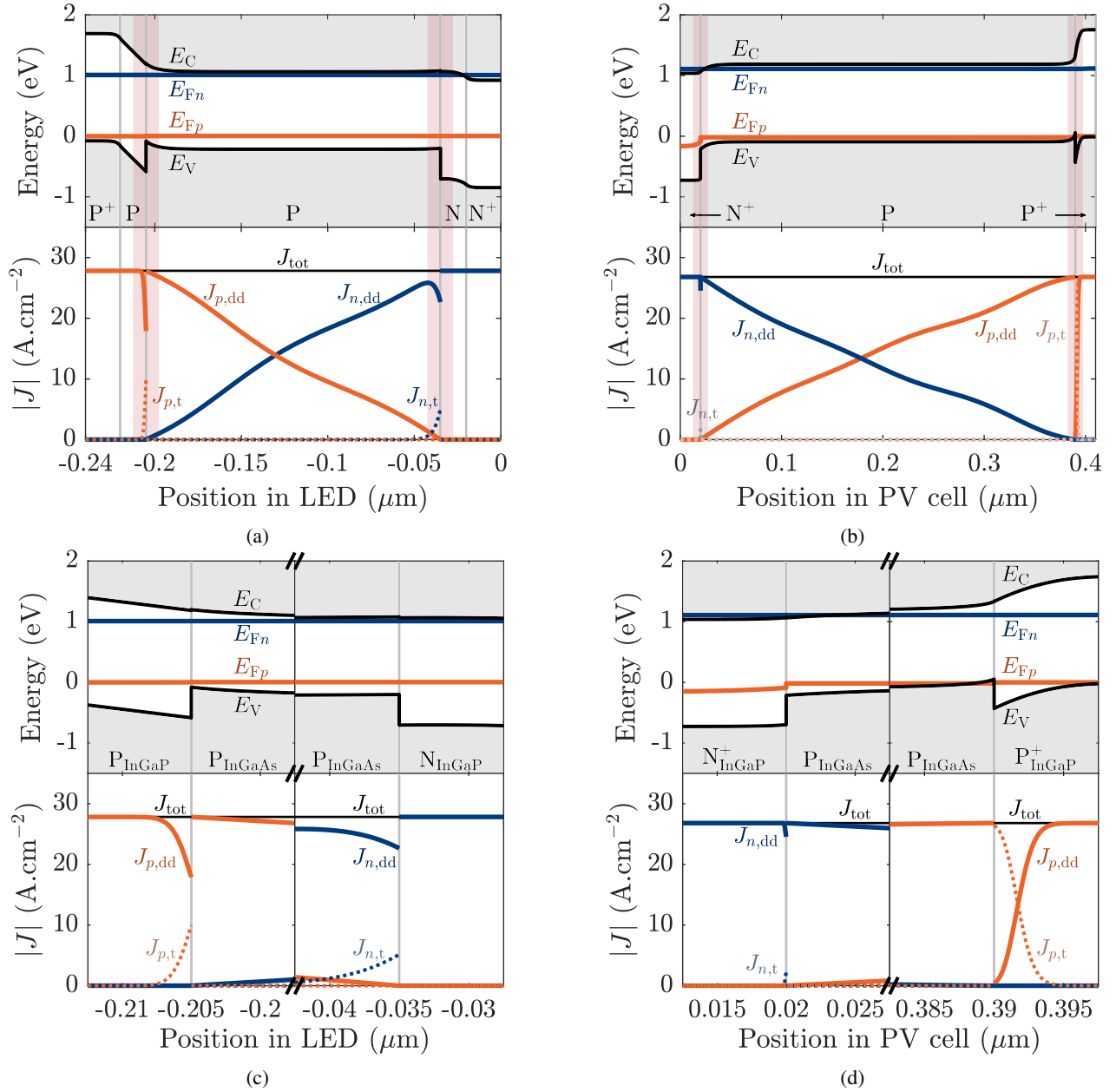


Fig. 3: Band diagram and spatial variation of electrical current densities (a) in the LED, (b) in the PV cell, at TPX maximum power point. Panels (c,d) are respective zooms of panels (a,b) close to the heterointerfaces (coloured areas). Results obtained for $d = 10$ nm and $T_h = 600$ K.

maximum power point (MPP) in the following. Details on power-efficiency trade-off in TPX devices can be found e.g. in [1], [2], [18], [31].

To get an accurate description of one device over the complete voltage space, CRESCENT-1D takes one to two hours to solve the coupled radiative and electrical problem on a computer with a 10th generation Intel Core i5 processor and with 16 GB of RAM. This time depends on the number of layers present in each component, and on the precision of the various meshes. For preliminary calculations where precision is not required, the computational time can for instance be decreased to 3 minutes, at the cost of a 5-to-10% relative error on the maximum power output. More information on the mesh

sizes considered and on computational time can be found in Section IV of Supp. Mat.

In Section V of Supp. Mat. is shown a comparison of the results returned by CRESCENT-1D and by SCAPS [24] considering a simpler structure. The match between the two is almost perfect, only a slight mismatch being observable for low applied voltages, i.e. far from the MPP.

A. Band diagrams and local electrical current

The most detailed data available are the spatially-resolved band diagrams and current densities of each component, obtained for a given couple of applied voltages. They are

represented in Fig. 3 at the MPP. The location of the heterointerfaces is highlighted in red, and panels (c) and (d) provide a detailed view of the evolution of these quantities in the vicinity of the interfaces. The barrier height in the conduction and valence bands is respectively equal to $\Delta\chi$ and $\Delta\chi + \Delta E_g$. Since the electron affinity of InGaAs and InGaP are nearly equal, $\Delta\chi \approx 0$ and almost no barrier appears in the conduction band.

One can observe that the quasi-Fermi levels almost do not vary spatially: this highlights the excellent charge carrier separation, which is also reflected in the very low minority carrier current density close to the component boundaries. In regular PV textbooks, minority and majority carrier quasi-Fermi levels are often shown to coincide at the contacts [46]. This can only happen if minority carriers are at equilibrium with the majority ones; since here, we rather suppose that they recombine following Eq. (9), E_{Fn} and E_{Fp} are not expected to merge at the boundaries. Additionally, the quasi-Fermi levels are close to the two bands, even entering them in the N^+ layers. In such conditions, the semiconductor becomes degenerate and the Boltzmann approximation loses accuracy. In future work, it will be important to estimate this accuracy loss and to try to include the complete Fermi-Dirac distribution to the solver, for instance by multiplying the Slotboom variables by a corrective term $1/(1 + \Phi)$ which could be computed using the solution of the previous iteration.

For the current structure, only the PV cell hole quasi-Fermi level exhibits discontinuities at the heterointerface, and it does especially at the P-N interface. Still, the discontinuities are small, and one could therefore wonder if the simpler model of quasi-Fermi level continuity could suffice. However, charge carrier tunnelling would not be included in such a model, while it represents a significant transmission channel through all heterointerfaces (subscript “t” in panels (c) and (d) of Fig. 3). This is particularly true at the PV cell P-P junction, where almost all travelling holes tunnel through the barrier despite their high effective mass due to the height of the potential barrier. Therefore, we shall now compare the results provided by the different models, and analyse which ones are relevant for such structures.

B. Comparison of available models

1) *Heterointerface models*: We plot in panel (a) of Fig. 4 the variations of TPX maximum electrical power output with LED voltage obtained with each model. The “complete” scenario corresponds to the one considered previously, with both thermionic emission and tunnelling included. Such a figure highlights a difference in convergence between the three heterointerface models, with only the complete one being able to provide the complete electrical characteristic (i.e. up to $P(U_{LED}) = 0$). In comparison, the thermionic emission model starts to diverge around $U_{LED} = 0.8$ V. It may seem counterintuitive that this model diverges before the “continuity” one, although including a phenomenon that the latter does not. In fact, while including thermionic emission allows accounting for discontinuous quasi-Fermi levels, it tends to overestimate these discontinuities significantly in comparison

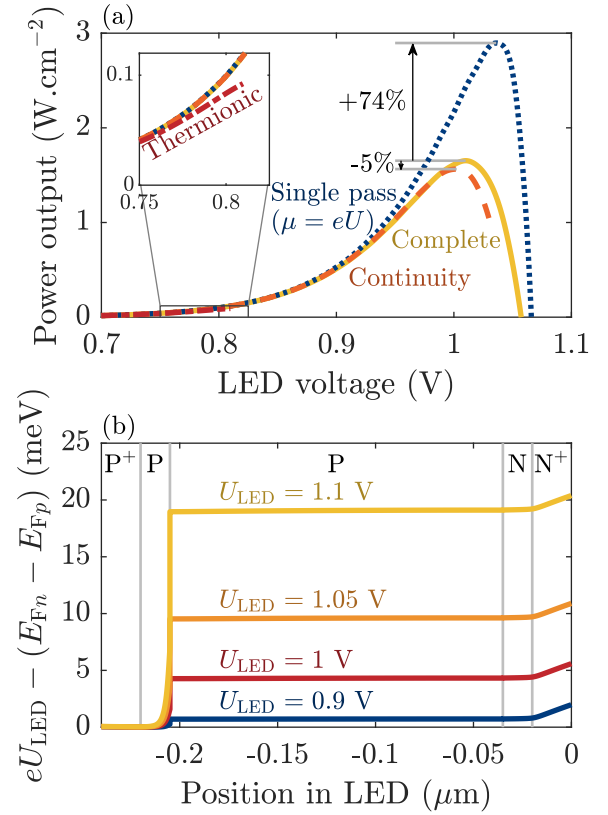


Fig. 4: (a) Comparison of the performance obtained for the TPX device of Fig. 1a with various models. The yellow curve represents the complete model, including thermionic emission and charge carrier tunnelling at heterointerfaces, along with an iterative calculation of μ . The orange and red curves represent approximated models of heterointerfaces, while the results in blue rely on the approximation $\mu = eU$ (single-pass model). (b) Deviation from the hypothesis $E_{Fn} - E_{Fp} = eU$ in the LED obtained with the complete model.

to the complete model. This is the main reason for the early divergence of the thermionic emission model, which makes it unsuitable for our solver.

Although it prematurely diverges, the continuity model is still able to describe the electrical characteristic up to the MPP, making the comparison with the complete model possible. Below $U_{LED} = 0.95$ V, the match between the two set of results is almost perfect. Indeed, for such voltages, current densities remain low enough for the discontinuity in quasi-Fermi levels to be negligible: the continuity model can then describe accurately charge transport, although it fails to depict how these charges truly travel through the heterointerfaces. However, near the MPP, these discontinuities start to play a role in the transport of electrons and holes, and the two electrical characteristics thus differ. The error made by the continuity model on the maximum power output is of the order of 5% for the system considered, and values up to 15% were observed for other structures. Therefore, the complete resolution should generally be preferred. Still, tunnelling probability is heavy to compute, and using the continuity approximation can allow dividing the computational time dedicated to the

electrical solver by a factor 2. This simpler model can therefore be suitable for preliminary calculations, although one should always verify that CRESCENT-1D then converges up to the MPP.

2) *Photon chemical potential model*: In Section II-C, we explained how the coupling implemented between the radiative and electrical solvers ensures self-consistency of the photon chemical potential. To quantify how such a self-consistent treatment impacts the results, we provide in panel (a) of Fig. 4 the electrical characteristic obtained after a single pass in the solver, i.e. considering the chemical potential of radiation to be eU . As for the continuity model, there is good agreement between the single-pass and the self-consistent models for voltages below $U_{\text{LED}} = 0.95$ V, while they fail to match for larger voltages. In this case, the mismatch is much more important, the self-consistent model overestimating the maximum power output by 74%.

This mismatch is again caused by the strong variations of the quasi-Fermi levels at and near the heterointerfaces. This can be observed in panel (b) of Fig. 4, where we display how far the true photon chemical potential $\mu = E_{F_n} - E_{F_p}$ is from eU . This is plotted for the LED only, since this is the component which drives the radiative heat transfer. First, one can observe that $E_{F_n} - E_{F_p}$ is mostly constant within each layer, especially in the active InGaAs layer in the middle which is the main emitting layer: this justifies the use of a unique value of μ for each layer to compute the radiative terms. The difference between $E_{F_n} - E_{F_p}$ and eU appears to be mostly caused by the change in $E_{F_n} - E_{F_p}$ close to the P-P heterojunction, whose amplitude increases exponentially with U_{LED} and becomes significant (i.e. non-negligible compared to the thermal energy $k_B T_h$) above 0.95 V. Although near the MPP, the difference between μ and eU is of the order of 10 to 20% of $k_B T_h$, this is enough to cause the large mismatch observed between the electrical characteristics, which highlights the need for self-consistently computing μ . This is a general conclusion of our work: because TPX systems must operate under high voltages to deliver high power output, thermionic emission and charge carrier tunnelling, which are usually negligible, are both to be accounted for, making some common models such as $\mu = eU$ unsuitable.

C. TPX device performance

Finally, we discuss the heat engine performance achieved by the optimised structure presented earlier. For $T_h = 600$ K, $T_c = 300$ K and a vacuum gap distance $d = 10$ nm, the TPX device is capable of delivering an electrical power density of 1.6 W.m^{-2} . This value is obtained considering a surface recombination velocity of 10^4 cm.s^{-1} which is realistic at the interface between metallic contacts and highly-doped InGaP [47] and for which the previously studied TPX homostructure was barely able to deliver power due to the limited separation of charge carriers [31]. The above-bandgap efficiency at maximum power, which is obtained by neglecting below-bandgap radiative heat transfer, reaches 19.7% and is several percent points higher than the values reported in the literature for NF-TPX systems including non-radiative losses

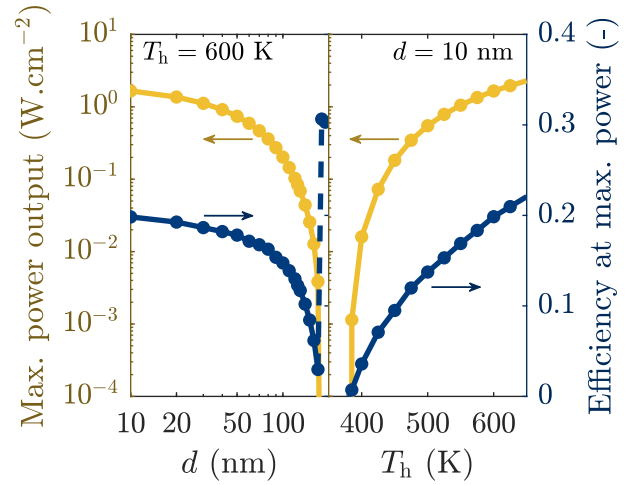


Fig. 5: Variation of the maximum power output and related efficiency achievable by the device from Fig. 1a, depending on (a) the vacuum gap distance, (b) the heat source temperature.

[12], [16], [18], [31]. For the low heat source temperature considered, such a high efficiency at maximum power can only be achieved by the excellent carrier selectivity and the significant reduction of the non-radiative recombination rate enabled by the use of heterostructures.

The variations of the maximum power output and of the related efficiency with the gap distance are illustrated in the left panel of Fig. 5. As the system moves towards far-field operation, one can observe that both quantities quickly decay, much quicker in fact than the thermal heat flux exchanged between the LED and the PV cell (which decreases only by a factor 8.5 from $d = 10$ nm to $d = 200$ nm). This is because near-field operation significantly improves the LED quantum efficiency (defined as r_{rad}/r) [48], thus the overall TPX performance; such an improvement is progressively lost as d increases [31]. Above 180 nm, the LED quantum efficiency becomes so low that TPV operation becomes preferable to TPX, causing a sudden drop in power output and a simultaneous increase in efficiency (dashed line). This highlights the importance of operating in the near field for TPX devices.

We also evaluated the impact of T_h on TPX performance, whose results are gathered on the right panel of Fig 5. To obtain these results, note that the InGaAs and InGaP In fraction have been varied so that the LED and PV cell active layers present matched bandgaps, and keep their lattice constant equal to that of surrounding InGaP layers. This prevents the power output from dropping quickly to zero due to bandgap mismatch between the active layers when T_h differs significantly from 600 K [12]. Close to $T_h = 600$ K, the power output varies moderately with temperature, reaching respectively 1.1 and 2.3 W.m^{-2} for $T_h = 550$ K and 650 K. Below 550 K however, it decreases dramatically and eventually reaches 0 for a temperature close to 380 K: non-radiative losses then prevail and do not allow any power production. This highlights the difficulty of achieving high-power TPX for heat source temperature close to ambient, along with the need for further development in that matter.

IV. CONCLUSION

In this paper, we have introduced CRESCENT-1D, the one-dimensional solver we developed to estimate the performance of near-field thermophotonic devices. It is the first publicly available algorithm capable of coupling near-field radiative heat transfer and charge transport for thermophotonic systems. Because heterojunctions can be much more efficient optoelectronic converters than homojunctions are, we have sought to precisely model how charge carriers behave in such structures by including both thermionic emission and tunnelling. This, along with the self-consistent calculation of the photon chemical potential, has proved to be essential to precisely obtain the complete electrical characteristic of devices.

CRESCENT-1D can provide a wide variety of information concerning light and charge transport: e.g., the radiative heat flux exchanged between the two components, their band diagrams, their spatially-resolved currents and recombination-generation rates, or their electrical characteristic. Such quantities give insights on the main physical phenomena at work, on the main sources of losses, and on possible ways to mitigate them. Used with an optimisation process, it is also able to provide promising structures, such as the one we have presented above, which reaches a power output of 1.6 W.m^{-2} and a related efficiency of 19.7% for a temperature difference of 300 K. This will be of great help for the design of TPX devices.

Although such a temperature difference is common in TPX literature, follow-up studies shall focus on optimising structures for lower ΔT , in particular for $\Delta T < 100 \text{ K}$ where most of the waste heat lies [49]. Moreover, as mentioned earlier, some loss phenomena - such as resistive losses [23] or parasitic absorption - are not included in the solver yet, while the non-radiative recombination coefficients used lack precision due to the absence of reliable temperature-dependent data for binary and ternary III-V semiconductors. This, along with the correction of the Boltzmann approximation into the complete Fermi-Dirac distribution, shall be addressed to better represent real devices.

As a final comment, we shall mention that voltages and currents of the two optoelectronic components do not match, and the system would therefore need external electronics to work. In the future, there would be great interest in designing 1D self-sustaining devices, which no longer need such external systems [14], [50].

ACKNOWLEDGEMENTS

The authors thank T. Châtelet, P. Kivisaari, O. Merchiers, J. Oksanen and J. van Gastel.

REFERENCES

- [1] J. Legendre and P.-O. Chapuis, "Operating conditions and thermodynamic bounds of dual radiative heat engines," Feb. 2024.
- [2] N.-P. Harder and M. A. Green, "Thermophotonics," *Semiconductor Science and Technology*, vol. 18, no. 5, pp. S270–S278, May 2003.
- [3] G. C. Dousmanis, C. W. Mueller, H. Nelson, and K. G. Petzinger, "Evidence of Refrigerating Action by Means of Photon Emission in Semiconductor Diodes," *Physical Review*, vol. 133, no. 1A, pp. A316–A318, Jan. 1964.
- [4] P. Santhanam, D. J. Gray, and R. J. Ram, "Thermoelectrically Pumped Light-Emitting Diodes Operating above Unity Efficiency," *Physical Review Letters*, vol. 108, no. 9, p. 097403, Feb. 2012.
- [5] X. Liu and Z. M. Zhang, "High-performance electroluminescent refrigeration enabled by photon tunneling," *Nano Energy*, vol. 26, pp. 353–359, Aug. 2016.
- [6] T. Sadi, I. Radevici, and J. Oksanen, "Thermophotonic cooling with light-emitting diodes," *Nature Photonics*, vol. 14, no. 4, pp. 205–214, Apr. 2020.
- [7] R. Sakakibara, V. Stelmakh, W. R. Chan, M. Ghebrebrhan, J. D. Joannopoulos, M. Soljačić, and I. Čelanović, "Practical emitters for thermophotovoltaics: A review," *Journal of Photonics for Energy*, vol. 9, no. 03, p. 1, Feb. 2019.
- [8] T. Burger, C. Sempere, B. Roy-Layinde, and A. Lenert, "Present Efficiencies and Future Opportunities in Thermophotovoltaics," *Joule*, vol. 4, no. 8, pp. 1660–1680, 2020.
- [9] A. LaPotin, K. L. Schulte, M. A. Steiner, K. Buznitsky, C. C. Kelsall, D. J. Friedman, E. J. Tervo, R. M. France, M. R. Young, A. Rohskopf, S. Verma, E. N. Wang, and A. Henry, "Thermophotovoltaic efficiency of 40%," *Nature*, vol. 604, no. 7905, pp. 287–291, Apr. 2022.
- [10] E. J. Tervo, R. M. France, D. J. Friedman, M. K. Arulanandam, R. R. King, T. C. Narayan, C. Luciano, D. P. Nizamian, B. A. Johnson, A. R. Young, L. Y. Kuritzky, E. E. Perl, M. Limpinsel, B. M. Kayes, A. J. Ponec, D. M. Bierman, J. A. Briggs, and M. A. Steiner, "Efficient and scalable GaInAs thermophotovoltaic devices," *Joule*, vol. 6, no. 11, pp. 2566–2584, Nov. 2022.
- [11] I. Tobias and A. Luque, "Ideal efficiency and potential of solar thermophotonic converters under optically and thermally concentrated power flux," *IEEE Transactions on Electron Devices*, vol. 49, no. 11, pp. 2024–2030, Nov. 2002.
- [12] B. Zhao, P. Santhanam, K. Chen, S. Buddhiraju, and S. Fan, "Near-Field Thermophotonic Systems for Low-Grade Waste-Heat Recovery," *Nano Letters*, vol. 18, no. 8, pp. 5224–5230, Aug. 2018.
- [13] S. McSherry, T. Burger, and A. Lenert, "Effects of narrowband transport on near-field and far-field thermophotonic conversion," *Journal of Photonics for Energy*, vol. 9, no. 03, p. 1, Mar. 2019.
- [14] B. Zhao, S. Buddhiraju, P. Santhanam, K. Chen, and S. Fan, "Self-sustaining thermophotonic circuits," *Proceedings of the National Academy of Sciences*, vol. 116, no. 24, pp. 11 596–11 601, Jun. 2019.
- [15] Z. Yang, J. Wang, J. Guo, G. Lin, and J. Chen, "Parametric Optimum Design and Performance Improvement of a Thermophotonic Cell," *IEEE Transactions on Electron Devices*, vol. 67, no. 6, pp. 2376–2380, Jun. 2020.
- [16] Y. Matsuno, N. Nagumo, M. Araki, K. Yada, K. Yamaga, and A. Sakurai, "Non-equilibrium mid-infrared black phosphorus light emitter and absorber for thermophotonic applications," *Journal of Quantitative Spectroscopy and Radiative Transfer*, vol. 288, p. 108271, Sep. 2022.
- [17] T. Sadi, I. Radevici, B. Behaghel, and J. Oksanen, "Prospects and requirements for thermophotonic waste heat energy harvesting," *Solar Energy Materials and Solar Cells*, vol. 239, no. February, p. 111635, Jun. 2022.
- [18] F. Yang, K. Chen, Y. Zhao, S.-K. Kim, X. Luo, and R. Hu, "Near-field thermophotonic system for power generation and electroluminescent refrigeration," *Applied Physics Letters*, vol. 120, no. 5, p. 053902, Jan. 2022.
- [19] D. Polder and M. Van Hove, "Theory of Radiative Heat Transfer between Closely Spaced Bodies," *Physical Review B*, vol. 4, no. 10, pp. 3303–3314, Nov. 1971.
- [20] Z. M. Zhang, *Nano/Microscale Heat Transfer*, ser. Mechanical Engineering Series. Cham: Springer International Publishing, 2020.
- [21] D. Vasileska, S. M. Goodnick, and G. Klimeck, *Computational Electronics*. CRC Press, Dec. 2017.
- [22] E. Blandre, P.-O. Chapuis, and R. Vaillon, "High-injection effects in near-field thermophotovoltaic devices," *Scientific Reports*, vol. 7, p. 15860, Dec. 2017.
- [23] D. Milovich, J. Villa, E. Antolin, A. Datas, A. Marti, R. Vaillon, and M. Francoeur, "Design of an indium arsenide cell for near-field thermophotovoltaic devices," *Journal of Photonics for Energy*, vol. 10, no. 02, p. 1, Jun. 2020.
- [24] M. Burgelman, P. Nollet, and S. Degraeve, "Modelling polycrystalline semiconductor solar cells," *Thin Solid Films*, vol. 361–362, pp. 527–532, Feb. 2000.
- [25] B. Gaury, Y. Sun, P. Bermel, and P. M. Haney, "Sesame: A 2-dimensional solar cell modeling tool," *Solar Energy Materials and Solar Cells*, vol. 198, no. May 2018, pp. 53–62, Aug. 2019.

- [26] E. C. Dumitrescu, M. M. Wilkins, and J. J. Krich, "Simudo: A device model for intermediate band materials," *Journal of Computational Electronics*, vol. 19, no. 1, pp. 111–127, Mar. 2020.
- [27] G. P. Forcade, C. E. Valdivia, S. Molesky, S. Lu, A. W. Rodriguez, J. J. Krich, R. St-Gelais, and K. Hinzer, "Efficiency-optimized near-field thermophotovoltaics using InAs and InAsSbP," *Applied Physics Letters*, vol. 121, no. 19, p. 193903, Nov. 2022.
- [28] "Sentaurus Device - Technology Computer Aided Design (TCAD)," <https://www.synopsys.com/manufacturing/tcad/device-simulation/sentaurus-device.html>.
- [29] "Silvaco - TCAD - Device Simulation," <https://silvaco.com/tcad/victory-device-3d/>.
- [30] J. Legendre and P.-O. Chapuis, "GaAs-based near-field thermophotonic devices: Approaching the idealized case with one-dimensional PN junctions," *Solar Energy Materials and Solar Cells*, vol. 238, p. 111594, May 2022.
- [31] —, "Overcoming non-radiative losses with AlGaAs PIN junctions for near-field thermophotonic energy harvesting," *Applied Physics Letters*, vol. 121, no. 19, p. 193902, Nov. 2022.
- [32] W. A. Callahan, D. Feng, Z. M. Zhang, E. S. Toberer, A. J. Ferguson, and E. J. Tervo, "Coupled Charge and Radiation Transport Processes in Thermophotovoltaic and Thermoradiative Cells," *Physical Review Applied*, vol. 15, no. 5, p. 054035, May 2021.
- [33] M. Francoeur, M. Pinar Mengüç, and R. Vaillon, "Solution of near-field thermal radiation in one-dimensional layered media using dyadic Green's functions and the scattering matrix method," *Journal of Quantitative Spectroscopy and Radiative Transfer*, vol. 110, no. 18, pp. 2002–2018, Dec. 2009.
- [34] K. Joulain, "Near-field heat transfer: A radiative interpretation of thermal conduction," *Journal of Quantitative Spectroscopy and Radiative Transfer*, vol. 109, no. 2, pp. 294–304, Jan. 2008.
- [35] P.-O. Chapuis, S. Volz, C. Henkel, K. Joulain, and J. J. Greffet, "Effects of spatial dispersion in near-field radiative heat transfer between two parallel metallic surfaces," *Physical Review B*, vol. 77, no. 3, pp. 1–9, 2008.
- [36] J. Slotboom, "Computer-aided two-dimensional analysis of bipolar transistors," *IEEE Transactions on Electron Devices*, vol. 20, no. 8, pp. 669–679, Aug. 1973.
- [37] J. Legendre, "Theoretical and numerical analysis of near-field thermophotonic energy harvesters," Ph.D. dissertation, INSA Lyon, 2023.
- [38] M. S. Lundstrom and R. Schuelke, "Modeling semiconductor heterojunctions in equilibrium," *Solid-State Electronics*, vol. 25, no. 8, pp. 683–691, Aug. 1982.
- [39] C. Wu and E. Yang, "Carrier transport across heterojunction interfaces," *Solid-State Electronics*, vol. 22, no. 3, pp. 241–248, Mar. 1979.
- [40] K. Yang, J. R. East, and G. I. Haddad, "Numerical modeling of abrupt heterojunctions using a thermionic-field emission boundary condition," *Solid-State Electronics*, vol. 36, no. 3, pp. 321–330, Mar. 1993.
- [41] A. A. Grinberg and S. Luryi, "On electron transport across interfaces connecting materials with different effective masses," *IEEE Transactions on Electron Devices*, vol. 45, no. 7, pp. 1561–1568, Jul. 1998.
- [42] J. Verschraegen and M. Burgelman, "Numerical modeling of intra-band tunneling for heterojunction solar cells in scaps," *Thin Solid Films*, vol. 515, no. 15, pp. 6276–6279, May 2007.
- [43] D. Scharfetter and H. Gummel, "Large-signal analysis of a silicon Read diode oscillator," *IEEE Transactions on Electron Devices*, vol. 16, no. 1, pp. 64–77, Jan. 1969.
- [44] J. DeSutter, R. Vaillon, and M. Francoeur, "External Luminescence and Photon Recycling in Near-Field Thermophotovoltaics," *Physical Review Applied*, vol. 8, no. 1, p. 014030, Jul. 2017.
- [45] A. De Vos, *Endoreversible Thermodynamics of Solar Energy Conversion*. Oxford University Press, 1992.
- [46] P. Würfel and U. Würfel, *Physics of Solar Cells*. Wiley, Jan. 2016.
- [47] M. Levinshtein, S. Rumyantsev, and M. Shur, *Handbook Series on Semiconductor Parameters, Vol. 2—Ternary and Quaternary III-V Compounds*. World Scientific, Nov. 1999.
- [48] G. T. Papadakis, M. Orenstein, E. Yablonovitch, and S. Fan, "Thermodynamics of Light Management in Near-Field Thermophotovoltaics," *Physical Review Applied*, vol. 16, no. 6, p. 064063, 2021.
- [49] C. Forman, I. K. Muritala, R. Pardemann, and B. Meyer, "Estimating the global waste heat potential," *Renewable and Sustainable Energy Reviews*, vol. 57, pp. 1568–1579, 2016.
- [50] Z. Yang, J. Song, and B. J. Lee, "Thermophotonic cells in self-sustaining parallel circuits," *Journal of Quantitative Spectroscopy and Radiative Transfer*, vol. 312, p. 108792, Jan. 2024.